



# Vibration analysis of rotating pre-twisted blades

Hong Hee Yoo<sup>a,\*</sup>, Jung Hun Park<sup>b</sup>, Janghyun Park<sup>a</sup>

<sup>a</sup> Department of Mechanical Engineering, Hanyang University, Sungdong-Gu, Haengdang-Dong 17, Seoul 133-791, South Korea

<sup>b</sup> Department of Research Center, Functionbay Inc., Sangjin B/D 4F, Gangnam-Gu, Dogok-Dong 417, Seoul 135-270, South Korea

Received 10 November 2000; accepted 27 June 2001

---

## Abstract

Equations of motion for the vibration analysis of rotating pre-twisted blades are derived from a modelling method which employs hybrid deformation variables. The derived equations are transformed into dimensionless forms in which dimensionless parameters are identified. The effects of the dimensionless parameters on the modal characteristics of rotating pre-twisted blades are investigated. In particular, eigenvalue loci veering phenomena and associated mode shape variations are observed and discussed in this work. © 2001 Elsevier Science Ltd. All rights reserved.

**Keywords:** Vibration; Pre-twisted; Rotating blade; Stiffening effect; Loci veering; Dimensionless parameters; Mode shapes

---

## 1. Introduction

Rotating structures having the shape of pre-twisted blades commonly occur in several types of engineering structures such as turbines, turbomachines, and aircraft rotary wings. In order to design the rotating structures properly, their modal characteristics must be estimated accurately. The modal characteristics of rotating structures often vary significantly due to the effect of the centrifugal inertia force induced by the rotating motion. For this reason, the modal characteristics of rotating structures have been investigated by many researchers in the past.

An analytical method to calculate the natural frequencies of a rotating beam was presented by Southwell and Gough [1]. They proposed an equation which related the natural frequency to the rotating frequency of a beam. This equation, which is frequently called the Southwell equation has been widely used because it is simple and easy to use. To obtain more accurate natural frequencies, a linear partial differential equation that governs the bending vibration of a rotating beam was derived by Schilhansl [2]. Applying the Ritz method to

this partial differential equation, more accurate coefficients used in the Southwell equations were obtained. In 1970s, a large number of papers which employ numerical methods for the modal analysis of rotating structures have been published. For instance, Putter and Manor [3] applied the assumed mode approximation method for the modal analysis of a rotating beam. Various effects were also investigated. The effect of tip mass was considered by Hoa [4] and Wright et al. [5], elastic foundation and cross-section variation were considered by Kuo et al. [6], shear deformation was considered by Yokoyama [7], and the gyroscopic damping effect on the modal characteristics of a rotating beam was considered by Yoo and Shin [8]. A large number of related papers were reviewed by some researchers (see, for instance, Refs. [9,10]).

The effect of a pre-twist angle on the modal characteristics of a blade was studied by Carnegie and Thomas [11] and Dokumaci et al. [12]. However, the effect produced by rotational motion of the blade was not considered in these studies. Ramamurti and Kielb [13] employed a plate theory to calculate the natural frequencies of rotating pre-twisted blades. Since they employed a plate theory, a small principal area moment of inertia ratio was used for the numerical results. Moreover, relatively slow angular speed ratios were used to obtain their numerical results.

---

\* Corresponding author. Fax: +82-2-2293-5070.

E-mail address: hhyoo@email.hanyang.ac.kr (H.H. Yoo).

In the present study, the equations of motion to analyse the modal characteristics of rotating pre-twisted blades are derived from a modelling method which employs hybrid deformation variables. The use of hybrid deformation variables, which distinguishes the present modelling method from other conventional modelling methods, is the key ingredient used to derive the equations of motion rigorously. The integrity of the modelling method that employs hybrid deformation variables was first confirmed in Ref. [14], where only transient analysis results were presented. The same modelling method is employed in the present study for the modal analysis of rotating pre-twisted blades. In particular, eigenvalue loci veering phenomena and associated mode shape variations are introduced.

## 2. Equations of motion

### 2.1. Assumption and system configuration

The following assumptions are made in this study: first, the blade is composed of a homogeneous, isotropic material; second, the pre-twist rate of the blade along its longitudinal axis is uniform; third, the blade has slender shape so that shear and rotary inertia effects are negligible; fourth, gyroscopic coupling between the stretching and the bending motions are negligible as well; fifth, the neutral and centroidal axes in the cross-section of the blade coincide so that neither eccentricity nor torsion need be considered; lastly, no external force acts on the blade.

Fig. 1 shows the configuration of a uniformly pre-twisted blade.  $\alpha$  is the pre-twisted angle of the free end (where  $\hat{b}_1$ ,  $\hat{b}_2$ , and  $\hat{b}_3$  are attached) with respect to the fixed end (where  $\hat{a}_1$ ,  $\hat{a}_2$ , and  $\hat{a}_3$  are attached). Thus,  $\hat{b}_1 = \hat{a}_1$  and  $\hat{a}_2 \cdot \hat{b}_2 = \cos \alpha$ . Fig. 2 shows the deformation of the neutral axis of the blade. A generic point  $P_0$  which

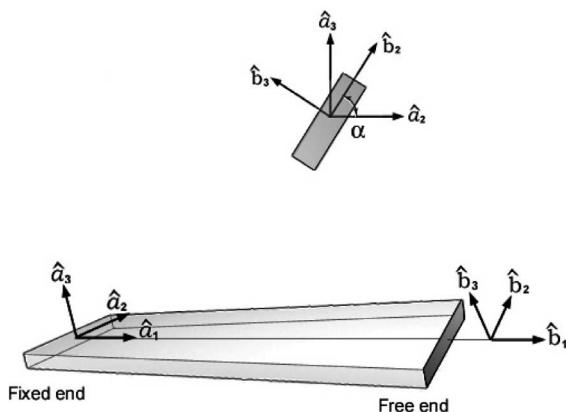


Fig. 1. Configuration of a pre-twisted blade.

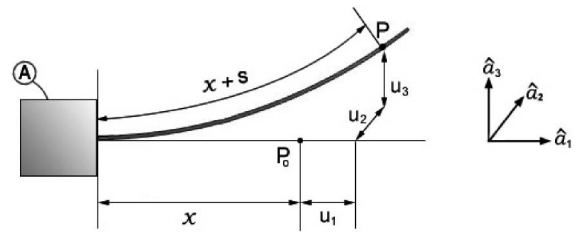


Fig. 2. Deformation of the blade neutral axis.

lies on the undeformed neutral axis moves to  $P$  when the blade is deformed. Three Cartesian variables  $u_1$ ,  $u_2$ , and  $u_3$  are shown to describe the deformation. The stretch of the arc length of the neutral axis,  $s$ , is also shown in the figure.

### 2.2. Approximation of deformation variables and strain energy expression

In the present study,  $s$ ,  $u_2$  and  $u_3$  are approximated by using spatial functions and corresponding coordinates in order to derive the ordinary differential equations of motion. The modelling method of using hybrid deformation variables is described in detail in Ref. [14]. By employing the Rayleigh Ritz method, the deformation variables are approximated as follows:

$$s(x, t) = \sum_{i=1}^{\mu_1} \phi_{1i}(x) q_{1i}(t) \quad (1)$$

$$u_2(x, t) = \sum_{i=1}^{\mu_2} \phi_{2i}(x) q_{2i}(t) \quad (2)$$

$$u_3(x, t) = \sum_{i=1}^{\mu_3} \phi_{3i}(x) q_{3i}(t) \quad (3)$$

where  $\phi_{1i}$ ,  $\phi_{2i}$ , and  $\phi_{3i}$  are the spatial functions for  $s$ ,  $u_2$  and  $u_3$ ; and  $\mu_1$ ,  $\mu_2$ , and  $\mu_3$  are the numbers of the generalized coordinates  $q_{1i}$ ,  $q_{2i}$ , and  $q_{3i}$ . There is an approximate geometric relation (see Ref. [14]) between the arc length stretch and the Cartesian variables, given by

$$s = u_1 + \frac{1}{2} \int_0^x \left[ \left( \frac{\partial u_2}{\partial \sigma} \right)^2 + \left( \frac{\partial u_3}{\partial \sigma} \right)^2 \right] d\sigma \quad (4)$$

Since the arc length stretch  $s$  instead of  $u_1$  is approximated in this study, Eq. (4) is used to obtain generalized inertia forces in the equations of motion. Since linear equations of motion are to be eventually derived, the truncation involved in the approximate relation does not affect the final results of the derived equations.

Using the stretch of the arc length, the precise stretching strain energy can be expressed in a quadratic

form. Thus, the total strain energy can be described as follows:

$$U = \frac{1}{2} \int_0^L \left[ EA \left( \frac{\partial s}{\partial x} \right)^2 + EI_3 \left( \frac{\partial^2 u_2}{\partial x^2} \right)^2 + EI_2 \left( \frac{\partial^2 u_3}{\partial x^2} \right)^2 + 2EI_{23} \left( \frac{\partial^2 u_2}{\partial x^2} \right) \left( \frac{\partial^2 u_3}{\partial x^2} \right) \right] dx \quad (5)$$

where  $E$  is Young's modulus;  $A$  is the cross-sectional area;  $I_2$ ,  $I_3$  and  $I_{23}$  are the second area moments of inertia and the second area product of inertia of the cross-section respectively; and  $L$  is the length of the blade. By using  $I_2^*$  and  $I_3^*$ , the principal second area moments of the cross-section,  $I_2$ ,  $I_3$  and  $I_{23}$  can be expressed as follows:

$$I_2(x) = \frac{I_2^* + I_3^*}{2} + \frac{I_2^* - I_3^*}{2} \cos(2\theta) \quad (6)$$

$$I_3(x) = \frac{I_2^* + I_3^*}{2} - \frac{I_2^* - I_3^*}{2} \cos(2\theta) \quad (7)$$

$$I_{23}(x) = \frac{I_2^* - I_3^*}{2} \sin(2\theta) \quad (8)$$

where

$$\theta \equiv \alpha \frac{x}{L} \quad (9)$$

In Eqs. (6)–(9),  $\theta$  is the pre-twist angle of a cross-section with respect to the fixed end. Thus,  $\theta = 0$  at the fixed end and  $\theta = \alpha$  at the free end.

### 2.3. Equations of motion

Under the assumptions described in Section 2.1, the equations of motion can be obtained from the following equation (see Ref. [15]).

$$\int_0^L \rho \vec{a}^P \cdot \left( \frac{\partial \vec{v}^P}{\partial \dot{q}_i} \right) dx + \frac{\partial U}{\partial \dot{q}_i} = 0 \quad (i = 1, 2, \dots, \mu) \quad (10)$$

where  $\rho$  is the mass per unit length of the blade;  $q_i$ 's are composed of the generalized coordinates  $q_{1i}$ ,  $q_{2i}$ , and  $q_{3i}$ ; and  $\vec{v}^P$  and  $\vec{a}^P$  are the velocity and the acceleration of the generic point  $P$ . The acceleration can be obtained by differentiating the velocity  $\vec{v}^P$  with respect to time, which can be obtained by using the following equation.

$$\vec{v}^P = \vec{v}^O + \frac{d\vec{p}}{dt} + \vec{\omega}^A \times \vec{p} \quad (11)$$

where  $\vec{v}^O$  is the velocity of point  $O$  that is fixed to the rigid hub;  $\vec{\omega}^A$  is the angular velocity of the rigid hub; and  $\vec{p}$  is the vector from point  $O$  to point  $P$ . The second term in the right-hand side of Eq. (11) denotes the time differentiation of vector  $\vec{p}$  in the reference frame  $A$  (the

rigid hub). Using the coordinate systems fixed to the rigid hub,  $\vec{v}^O$ ,  $\vec{\omega}^A$ , and  $\vec{p}$  can be expressed as follows:

$$\vec{v}^O = r\Omega\hat{a}_2 \quad (12)$$

$$\vec{\omega}^A = \Omega\hat{a}_3 \quad (13)$$

$$\vec{p} = (x + u_1)\hat{a}_1 + u_2\hat{a}_2 + u_3\hat{a}_3 \quad (14)$$

where  $r$  is the radius of the rigid hub (i.e. distance from rotation centre to point  $O$ ) and  $\Omega$  is the angular speed of the rigid hub. The velocity of point  $P$  can be obtained as follows:

$$\vec{v}^P = [\dot{u}_1 - \Omega u_2]\hat{a}_1 + [\dot{u}_2 + \Omega(r + x + u_1)]\hat{a}_2 + \dot{u}_3\hat{a}_3 \quad (15)$$

To derive the equations of motion, the partial velocities of  $P$  (the partial derivatives of the velocity of  $P$  with respect to the generalized speed  $\dot{q}_i$ 's) must be obtained. Thus,

$$\frac{\partial \vec{v}^P}{\partial \dot{q}_{1i}} = \phi_{1i}\hat{a}_1 \quad (i = 1, 2, \dots, \mu_1) \quad (16)$$

$$\frac{\partial \vec{v}^P}{\partial \dot{q}_{2i}} = \left[ -\sum_{j=1}^{\mu_2} \left( \int_0^x \phi'_{2i}\phi'_{2j} d\sigma \right) q_{2j} \right] \hat{a}_1 + \phi_{2i}\hat{a}_2 \quad (i = 1, 2, \dots, \mu_2) \quad (17)$$

$$\frac{\partial \vec{v}^P}{\partial \dot{q}_{3i}} = \left[ -\sum_{j=1}^{\mu_3} \left( \int_0^x \phi'_{3i}\phi'_{3j} d\sigma \right) q_{3j} \right] \hat{a}_1 + \phi_{3i}\hat{a}_3 \quad (i = 1, 2, \dots, \mu_3) \quad (18)$$

where a symbol with a prime (') represents the partial derivative of the symbol with respect to the integral domain variable. By substituting the partial velocities and the strain energy expression of Eq. (5) into Eq. (10), the linearized equations of motion can be obtained as follows:

$$\sum_{j=1}^{\mu_1} M_{ij}^{11} \ddot{q}_{1j} + \sum_{j=1}^{\mu_1} \left\{ K_{ij}^S - \Omega^2 M_{ij}^{11} \right\} q_{1j} - 2\Omega \sum_{j=1}^{\mu_2} M_{ij}^{12} \dot{q}_{2j} = r\Omega^2 P_{1i} + \Omega^2 Q_{1i} \quad (19)$$

$$\sum_{j=1}^{\mu_2} M_{ij}^{22} \ddot{q}_{2j} + 2\Omega \sum_{j=1}^{\mu_1} M_{ij}^{21} \dot{q}_{1j} + \sum_{j=1}^{\mu_3} K_{ij}^{B23} q_{3j} + \sum_{j=1}^{\mu_2} \left\{ \Omega^2 (K_{ij}^{GB2} + rK_{ij}^{GA2} - M_{ij}^{22}) + K_{ij}^{B2} \right\} q_{2j} = 0 \quad (20)$$

$$\sum_{j=1}^{\mu_3} M_{ij}^{33} \ddot{q}_{3j} + \sum_{j=1}^{\mu_2} K_{ij}^{B32} q_{2j} + \sum_{j=1}^{\mu_3} \left\{ \Omega^2 (K_{ij}^{GB3} + rK_{ij}^{GA3}) + K_{ij}^{B3} \right\} q_{3j} = 0 \quad (21)$$

where

$$M_{ij}^{ab} \equiv \int_0^L \rho \phi_{ai} \phi_{bj} dx \quad (22)$$

$$K_{ij}^{GAa} \equiv \int_0^L \rho(L-x) \phi'_{ai} \phi'_{aj} dx \quad (23)$$

$$K_{ij}^{GBa} \equiv \int_0^L \frac{\rho}{2} (L^2 - x^2) \phi'_{ai} \phi'_{aj} dx \quad (24)$$

$$P_{1i} \equiv \int_0^L \rho \phi_{1i} dx \quad (25)$$

$$Q_{1i} \equiv \int_0^L \rho x \phi_{1i} dx \quad (26)$$

$$K_{ij}^S \equiv \int_0^L EA \phi'_{1i} \phi'_{1j} dx \quad (27)$$

$$K_{ij}^{B2} \equiv \int_0^L EI_3 \phi''_{2i} \phi''_{2j} dx \quad (28)$$

$$K_{ij}^{B3} \equiv \int_0^L EI_2 \phi''_{3i} \phi''_{3j} dx \quad (29)$$

$$K_{ij}^{Bab} \equiv \int_0^L EI_{23} \phi''_{ai} \phi''_{bj} dx \quad (30)$$

where a symbol with a double prime (") represents the second derivative of the symbol with respect to the integral domain variable.

The coupling effect between the stretching and the bending motions is ignored in this study. The coupling effect with regard to slender beams does not significantly affect the results (see Ref. [8]). When ignoring the coupling effect and the stretching equation, the equations of motion can be simplified as follows:

$$\sum_{j=1}^{\mu_2} M_{ij}^{22} \ddot{q}_{2j} + \sum_{j=1}^{\mu_3} K_{ij}^{B23} q_{3j} + \sum_{j=1}^{\mu_2} \left\{ \Omega^2 (K_{ij}^{GB2} + r K_{ij}^{GA2} - M_{ij}^{22}) + K_{ij}^{B2} \right\} q_{2j} = 0 \quad (31)$$

$$\sum_{j=1}^{\mu_3} M_{ij}^{33} \ddot{q}_{3j} + \sum_{j=1}^{\mu_2} K_{ij}^{B32} q_{2j} + \sum_{j=1}^{\mu_3} \left\{ \Omega^2 (K_{ij}^{GB3} + r K_{ij}^{GA3}) + K_{ij}^{B3} \right\} q_{3j} = 0 \quad (32)$$

#### 2.4. Dimensionless equations of motion

To lend generality to the numerical results, Eqs. (31) and (32) are to be transformed into dimensionless

equations. For this transformation, several dimensionless variables and parameters are defined as follows:

$$\tau \equiv \frac{t}{T} \quad (33)$$

$$\xi \equiv \frac{x}{L} \quad (34)$$

$$\vartheta_{ai} \equiv \frac{q_{ai}}{L} \quad (35)$$

$$\gamma \equiv \Omega T \quad (36)$$

$$\delta \equiv \frac{r}{L} \quad (37)$$

$$\kappa \equiv \frac{I_2^*}{I_3^*} \quad (38)$$

where  $T$  appearing in Eqs. (33) and (36) is defined as

$$T \equiv \sqrt{\frac{\rho L^4}{EI_3^*}} \quad (39)$$

The parameters  $\gamma$ ,  $\delta$ , and  $\kappa$  represent the angular speed ratio, the hub radius ratio, and the principal area moment of inertia ratio, respectively. By using the parameter defined in Eq. (38), Eqs. (6)–(8) can be expressed as

$$\frac{I_2}{I_3^*} = \frac{1}{2}(\kappa + 1) + \frac{1}{2}(\kappa - 1) \cos(2\alpha\xi) \quad (40)$$

$$\frac{I_3}{I_3^*} = \frac{1}{2}(\kappa + 1) - \frac{1}{2}(\kappa - 1) \cos(2\alpha\xi) \quad (41)$$

$$\frac{I_{23}}{I_3^*} = \frac{1}{2}(\kappa - 1) \sin(2\alpha\xi) \quad (42)$$

The dimensionless equations of motion are finally obtained by using the dimensionless variables and parameters defined in Eqs. (33)–(38).

$$\sum_{j=1}^{\mu_2} \bar{M}_{ij}^{22} \ddot{\vartheta}_{2j} + \sum_{j=1}^{\mu_3} \bar{K}_{ij}^{B23} \vartheta_{3j} + \sum_{j=1}^{\mu_2} \left[ \gamma^2 (\bar{K}_{ij}^{GB2} + \delta \bar{K}_{ij}^{GA2} - \bar{M}_{ij}^{22}) + \bar{K}_{ij}^{B2} \right] \vartheta_{2j} = 0 \quad (43)$$

$$\sum_{j=1}^{\mu_3} \bar{M}_{ij}^{33} \ddot{\vartheta}_{3j} + \sum_{j=1}^{\mu_2} \bar{K}_{ij}^{B32} \vartheta_{2j} + \sum_{j=1}^{\mu_3} \left[ \gamma^2 (\bar{K}_{ij}^{GB3} + \delta \bar{K}_{ij}^{GA3}) + \bar{K}_{ij}^{B3} \right] \vartheta_{3j} = 0 \quad (44)$$

where

$$\bar{M}_{ij}^{ab} \equiv \int_0^1 \psi_{ai} \psi_{bj} d\xi \quad (45)$$

$$\bar{K}_{ij}^{B2} \equiv \int_0^1 \left\{ \frac{1}{2}(\kappa + 1) - \frac{1}{2}(\kappa - 1) \cos(2\alpha\xi) \right\} \psi_{2i}'' \psi_{2j}'' d\xi \quad (46)$$

$$\bar{K}_{ij}^{B3} \equiv \int_0^1 \left\{ \frac{1}{2}(\kappa + 1) + \frac{1}{2}(\kappa - 1) \cos(2\alpha\xi) \right\} \psi_{3i}'' \psi_{3j}'' d\xi \quad (47)$$

$$\bar{K}_{ij}^{GAa} \equiv \int_0^1 (1 - \xi) \psi_{ai}' \psi_{aj}' d\xi \quad (48)$$

$$\bar{K}_{ij}^{GBa} \equiv \int_0^1 \frac{1}{2} (1 - \xi^2) \psi_{ai}' \psi_{aj}' d\xi \quad (49)$$

$$\bar{K}_{ij}^{Bab} \equiv \int_0^1 \frac{1}{2} (\kappa - 1) \sin(2\alpha\xi) \psi_{ai}'' \psi_{bj}'' d\xi \quad (50)$$

where  $\psi$  is a function of  $\xi$  rather than of  $x$ .

### 2.5. Modal formulation

Eqs. (43) and (44) are expressed in a matrix form as follows:

$$\mathbf{M}\ddot{\vartheta} + \mathbf{K}\vartheta = 0 \quad (51)$$

where

$$\mathbf{M} \equiv \begin{bmatrix} \bar{M}^{22} & 0 \\ 0 & \bar{M}^{33} \end{bmatrix} \quad (52)$$

$$\mathbf{K} \equiv \begin{bmatrix} \bar{K}^{22} & \bar{K}^{23} \\ \bar{K}^{32} & \bar{K}^{33} \end{bmatrix} \quad (53)$$

$$\vartheta \equiv \begin{Bmatrix} \vartheta_2 \\ \vartheta_3 \end{Bmatrix} \quad (54)$$

In Eqs. (52) and (54),  $\bar{M}^{22}$  and  $\vartheta_2$ , for instance, are matrices which are composed of elements  $\bar{M}_{ij}^{22}$  and  $\vartheta_{2j}$ , respectively. The sub-matrices appearing in Eq. (53) are defined as follows:

$$\bar{K}^{22} \equiv [\gamma^2(\bar{K}^{GB2} + \delta\bar{K}^{GA2} - \bar{M}^{22}) + \bar{K}^{B2}] \quad (55)$$

$$\bar{K}^{23} \equiv \bar{K}^{B23} \quad (56)$$

$$\bar{K}^{32} \equiv \bar{K}^{B32} \quad (57)$$

$$\bar{K}^{33} \equiv [\gamma^2(\bar{K}^{GB3} + \delta\bar{K}^{GA3}) + \bar{K}^{B3}] \quad (58)$$

The natural frequencies and the associated mode shapes can be obtained from solution of Eq. (51).

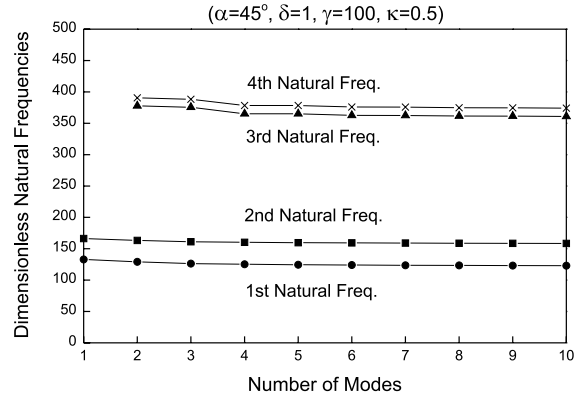


Fig. 3. Convergence of natural frequencies.

### 3. Numerical results

Fig. 3 shows the lowest four converging dimensionless natural frequencies for a rotating blade. A typical set of dimensionless parameters used for the simulation are shown in the figure. ‘Number of Modes’ in the figure represents the number of mode functions employed for each bending deflection. The lowest four natural frequencies obtained by employing nine modes are respectively compared with their corresponding natural frequencies obtained by employing 10 modes. The frequency gap in any of those four cases is less than 0.1% of the natural frequency obtained by employing 10 modes. Therefore, it is considered that the use of 10 modes is sufficient to obtain converged numerical results. So all the numerical results presented hereafter are obtained by using 10 modes.

The accuracy of the numerical results obtained by the present modelling method is examined first. In Table 1, the lowest four natural frequencies of a pre-twisted non-rotating blade are given, along with the dimensionless

Table 1  
Comparison of the lowest four natural frequencies ( $\gamma = 0.0$ ,  $\kappa = 0.25$ )

	$\alpha$	Present	Ref. [11]	Ref. [12]
First	30°	1.7623	1.7630	1.7620
	60°	1.7748	1.7737	1.7742
	90°	1.7950	1.7948	1.7949
Second	30°	3.4793	3.4788	3.4787
	60°	3.3799	3.3790	3.3790
	90°	3.2425	3.2422	3.2426
Third	30°	11.1693	11.1681	11.1698
	60°	11.6046	11.6025	11.6064
	90°	12.2649	12.2631	12.2611
Fourth	30°	21.4489	21.4451	21.4568
	60°	20.1545	20.1497	20.1769
	90°	18.7307	18.7246	18.7661

Table 2

Comparison of the lowest two natural frequencies ( $\alpha = 30^\circ$ ,  $\delta = 2.0$ ,  $\kappa = 1/400$ )

		First	Second
$\gamma = 0.0000$	Ref. [13]	0.1766	1.0001
	Present	0.1763	0.9825
$\gamma = 0.0882$	Ref. [13]	0.2217	1.0273
	Present	0.2200	1.0203
$\gamma = 0.1763$	Ref. [13]	0.3166	1.1321
	Present	0.3157	1.1254
$\gamma = 0.2645$	Ref. [13]	0.4277	1.2852
	Present	0.4288	1.2796

parameters used for the numerical results. The results obtained by using the present modelling method are compared with those presented in Refs. [11,12]. The maximum difference among the results is approximately 0.1%, which is equivalent to that obtained in the convergence study. In Table 2, the lowest two natural frequencies of a rotating pre-twisted blade are given. The results obtained by using the present modelling method are compared with those by a modelling method which employs a plate theory (see Ref. [13]). The dimensionless parameters employed for the numerical results are given in the table. The maximum difference between the two results is approximately 1.5%, which results from the difference between the beam theory and the plate theory.

The loci of lowest four natural frequencies of a rotating blade are shown in Fig. 4. The pre-twist angle of the blade is zero degree and the hub radius ratio is 1. The loci of the flapwise and the chordwise bending natural frequencies are drawn by dotted and solid lines, respectively. Since the principal area moment of inertia ratio ( $\kappa$ ) of the blade is  $>1$ , the flapwise bending natural frequencies are larger than the chordwise bending natural frequencies. Moreover, the increasing rate of the flapwise bending natural frequency is larger than that of

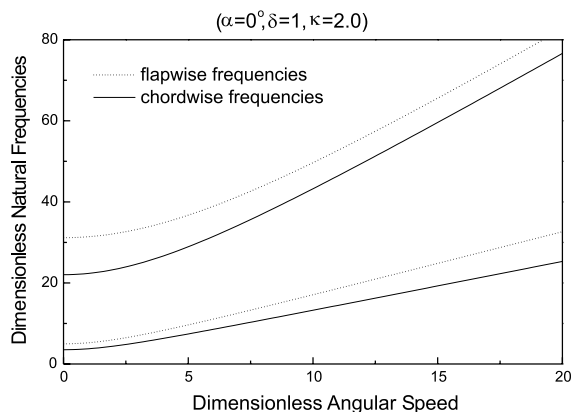


Fig. 4. No intersection of the four lowest natural frequency loci.

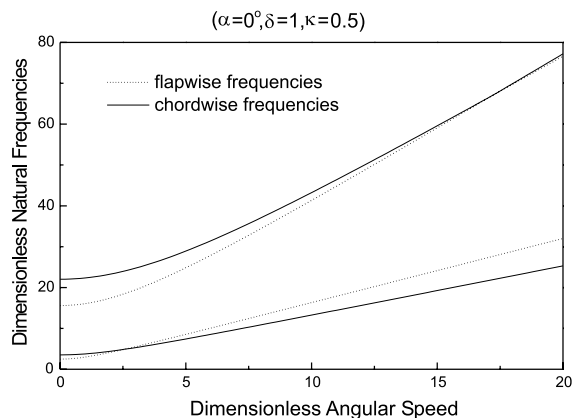


Fig. 5. Intersection of the four lowest natural frequency loci.

the chordwise bending natural frequency. Thus, their loci, as shown in the figure, do not intersect.

In Fig. 5, the loci of the lowest four natural frequencies of a rotating blade are shown. Different from the previous case, the principal area moment of inertia ratio is  $<1$ . Thus, the flapwise bending natural frequencies are smaller than the chordwise bending natural frequencies when the angular speed is zero. As the angular speed increases, the flapwise bending natural frequencies increase faster than the chordwise bending natural frequencies. Thus, they intersect as shown in the figure. The loci intersection, however, does not occur when the blade is pre-twisted. As shown in Fig. 6, the loci veer off rather than intersect. The veering phenomena were previously observed and discussed in other vibration problems (see, for instance, Ref. [16]), but they have not been discussed in blade vibration problems until now.

It is often difficult to distinguish a veering from an intersection when a veering occurs abruptly. To facilitate

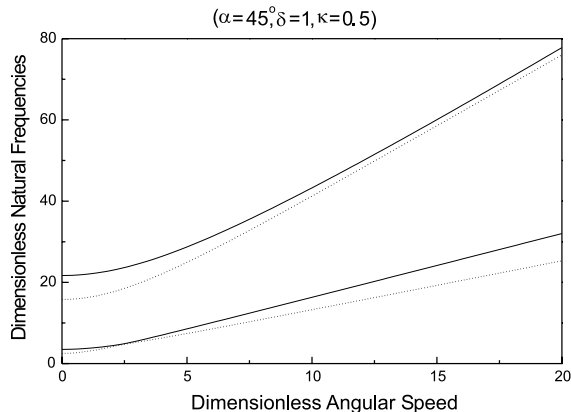


Fig. 6. Veering phenomena occurred with a non-zero pre-twist angle for the four lowest natural frequencies.

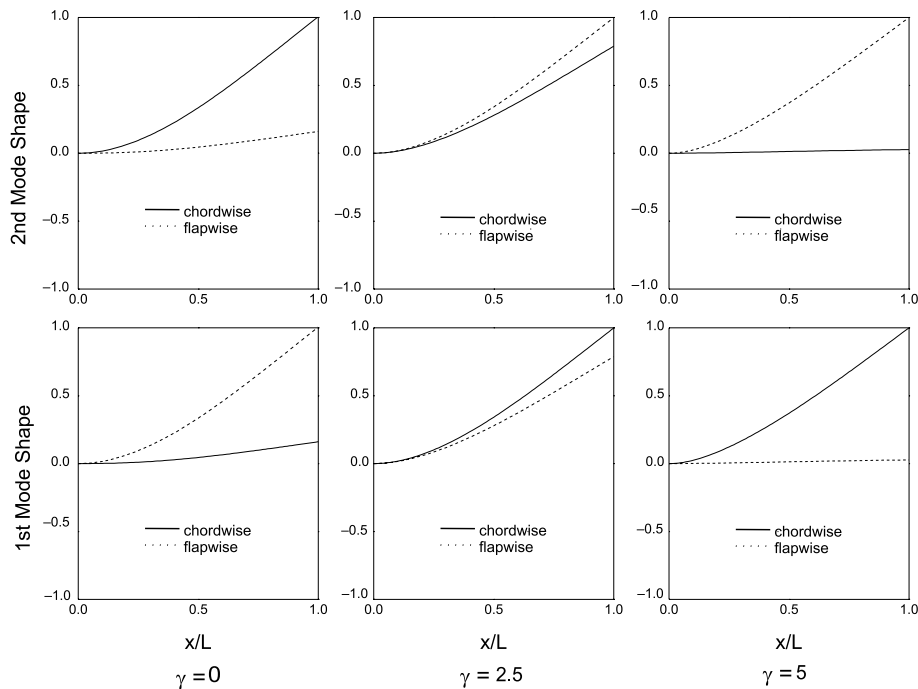


Fig. 7. Mode shape variations associated with loci veering.

this distinction, the veering (or intersecting) region should be magnified. In an intersection, the greater the magnification the closer the loci, whereas in a veering, magnifying a region makes little difference.

Fig. 7 shows the mode shape variations corresponding to the first and the second natural frequencies, which occur around the veering region shown in Fig. 6. The dotted and solid lines represent the magnitudes of the flapwise and the chordwise bending deflections, respectively. As shown in Fig. 7, the two mode shapes resemble each other as the two loci come closer. Then, the two mode shapes seem to be switched as the angular speed increases.

In Figs. 8 and 9, the loci of lowest two natural frequencies are shown. From the two figures, it is observed that the distance between the loci increases as the pre-twist angle increases. In other words, a mild veering occurs when the pre-twist angle is large enough whereas an abrupt veering occurs when the pre-twist angle is small.

When the angular speed of a rotating blade matches the natural frequency (as shown in Fig. 10), resonance may occur. Such an angular speed is usually called the tuned angular speed. Catastrophic failures often occur at the tuned angular speed during the operation of rotating blades. Thus, the tuned angular speed must be calculated for safe designs of rotating blades. The tuned angular speeds of rotating blades which have various dimensionless parameter values are tabulated in Tables 3

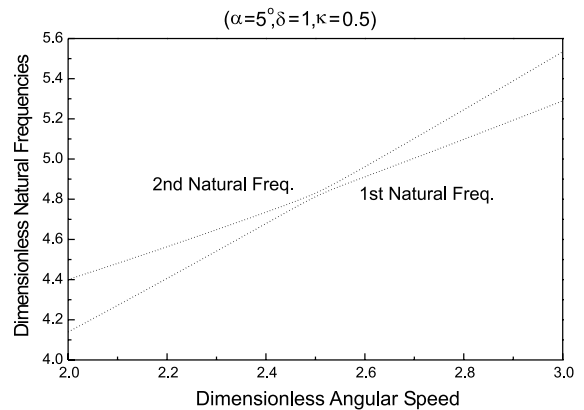


Fig. 8. Abrupt veering between the first and the second dimensionless natural frequencies.

and 4. The two tables (for different area moment of inertia ratios) show the variation of the tuned angular speed caused by the variations of the hub radius and the pre-twist angle. These results indicate that the hub radius ratio affects the tuned angular speed more significantly than the pre-twist angle does.

#### 4. Conclusions

In this study, the equations of motion for the vibration analysis of rotating pre-twisted blades are derived

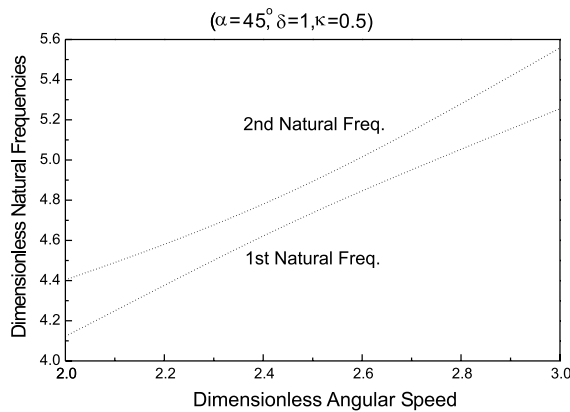


Fig. 9. Mild veering between the first and the second dimensionless natural frequencies.

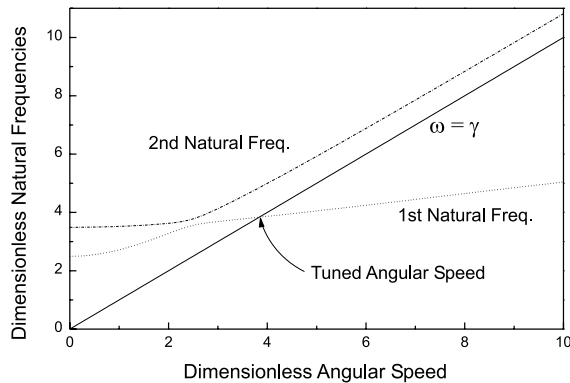


Fig. 10. Tuned angular speed at  $\alpha = 45^\circ$ ,  $\delta = 0$ , and  $\kappa = 0.5$ .

Table 3

Tuned angular speed versus hub radius ratio and pre-twist angle ( $\kappa = 0.5$ )

$\delta$	$\alpha = 0^\circ$	$\alpha = 15^\circ$	$\alpha = 30^\circ$	$\alpha = 45^\circ$
0.0	3.8744	3.8728	3.8591	3.8370
0.1	4.2934	4.2890	4.2763	4.2556
0.2	4.8686	4.8664	4.8528	4.8336
0.3	5.7294	5.7258	5.7152	5.6978
0.4	7.1871	7.1841	7.1749	7.1601
0.5	10.2666	10.2644	10.2571	10.2455

from a modelling method which employs hybrid deformation variables. The equations are transformed into dimensionless forms in which dimensionless parameters are identified. Numerical results obtained with the dimensionless equations are in good agreement with the

Table 4

Tuned angular speed versus hub radius ratio and pre-twist angle ( $\kappa = 2.0$ )

$\delta$	$\alpha = 0^\circ$	$\alpha = 15^\circ$	$\alpha = 30^\circ$	$\alpha = 45^\circ$
0.0	3.8774	3.8808	3.8907	3.9067
0.1	4.2934	4.2970	4.3078	4.3251
0.2	4.8686	4.8725	4.8842	4.9030
0.3	5.7294	5.7336	5.7460	5.7660
0.4	7.1817	7.1914	7.2040	7.2244
0.5	10.2666	10.2706	10.2825	10.3008

results reported in the literature. Numerical results also show that natural frequency loci veering phenomena occur when the blade is pre-twisted. The gap between the loci increases as the pre-twist angle increases. Mode shape variations associated with the loci veering phenomena are also exhibited and discussed. Lastly, the effects of the pre-twist angle and the hub radius ratio on tuned angular speeds (rotating frequencies which match the natural frequencies) are investigated. The results show that the hub radius significantly influences the tuned angular speed.

## Acknowledgements

This research was supported by Innovative Design Optimization Technology Engineering Research Center, for which authors are grateful.

## References

- [1] Southwell R, Gough F. The free transverse vibration of airscrew blades. British A.R.C. Reports and Memoranda no. 766, 1921.
- [2] Schilhansl M. Bending frequency of a rotating cantilever beam. J Appl Mech Trans Am Soc Mech Eng 1958;25:28–30.
- [3] Putter S, Manor H. Natural frequencies of radial rotating beams. J Sound Vib 1978;56:175–85.
- [4] Hoa S. Vibration of a rotating beam with tip mass. J Sound Vib 1979;67:369–81.
- [5] Wright A, Smith C, Thresher R, Wang J. Vibration modes of centrifugally stiffened beams. J Appl Mech 1982;49:197–202.
- [6] Kuo Y, Wu T, Lee S. Bending vibration of a rotating non-uniform beam with tip mass and an elastically restrained root. Comput Struct 1994;22:229–36.
- [7] Yokoyama T. Free vibration characteristics of rotating Timoshenko beams. Int J Mech Sci 1988;30:743–55.
- [8] Yoo H, Shin S. Vibration analysis of rotating cantilever beams. J Sound Vib 1998;212:807–28.
- [9] Leissa A. Vibration aspects of rotating turbomachinery blades. Appl Mech Rev 1981;34:629–35.



- [10] Rao J. Turbomachine blade vibration. *Shock Vib Dig* 1987;19:3–10.
- [11] Carnegie W, Thomas J. The coupled bending–bending vibration of pre-twisted tapered blading. *J Eng Indus* 1972;94:255–66.
- [12] Dokumaci E, Thomas J, Carnegie W. Matrix displacement analysis of coupled bending–bending vibrations of pre-twisted blading. *J Mech Eng Sci* 1967;9:247–51.
- [13] Ramamurti V, Kielb R. Natural frequencies of twisted rotating plates. *J Sound Vib* 1984;97:429–49.
- [14] Yoo H, Ryan R, Scott R. Dynamics of flexible beams undergoing overall motions. *J Sound Vib* 1995;181:261–78.
- [15] Kane T, Levinson D. *Dynamics: theory and application*. New York: McGraw-Hill; 1995.
- [16] Leissa A. On a curve veering aberration. *J Appl Math Phys (ZAMP)* 1974;25:99–111.